Enhanced memory capacity of a neuromorphic reservoir computing system based on a VCSEL with double optical feedbacks

Xingxing GUO[1], Shuiying XIANG[1,2*], Yahui ZHANG[1], Aijun WEN[1] & Yue HAO[2]

[1]*State Key Laboratory of Integrated Service Networks, Xidian University, Xi'an 710071, China;*
[2]*State Key Discipline Laboratory of Wide Bandgap Semiconductor Technology, School of Microelectronics, Xidian University, Xi'an 710071, China*

Abstract In this paper, a neuromorphic reservoir computing (RC) system with enhanced memory capacity (MC) based on a vertical-cavity surface-emitting laser (VCSEL) subject to double optical feedbacks (DOF) is proposed and investigated numerically. The aim of this study is to explore the MC of the proposed system. For the purpose of comparison, the MC of the VCSEL-based RC system with single optical feedback (SOF) is also taken into account. It is found that, compared with the VCSEL-based RC system subject to SOF, enhanced MC can be obtained for the VCSEL-based RC system with DOF. Besides, the effects of feedback strength, injected strength, frequency detuning as well as injection current on the MC of the VCSEL-based RC system with DOF are considered. Moreover, the influence of feedback delays is also carefully examined. Thus, such proposed VCSEL-based RC system with DOF provides a prospect for the further development of the neuromorphic photonic system based on RC.

Keywords vertical-cavity surface-emitting laser, nanophotonic reservoir computing, memory capacity, double feedback, information processing

1 Introduction

In today's era, information processing abilities have been improved unprecedentedly owing to the great increase of information. However, standard computers based on von Neumann architectures cannot efficiently solve certain tasks. New opportunities can be provided by unconventional computation schemes. Inspired by the brain's information processing patterns, reservoir computing (RC) as a neuromorphic computing scheme and simplified form of recurrent neural networks has been proposed [1, 2]. Using RC for speech recognition [3–6], nonlinear channel equalization [7,8], radar signal processing [9], classification of handwritten digits [10], and reconstruction of complex dynamical systems [11,12] have currently gained great interest.

In an RC system, the input weights and the reservoir internal weights are fixed randomly and only the output weights are trained by learning [13]. Recently, Appeltant et al. [14] proposed the concept of a virtual network for RC by adopting a single nonlinear node with delay feedback, which has opened a new field of time-delay RC. The implementations of such time-delay RC have been quickly demonstrated in a

---

* Corresponding author (email: jxxsy@126.com)

considerable number of electronic [14], optoelectronic [15,16] as well as all optical [5,17–23] delay systems. For example, Paquot et al. [16] reported an optoelectronic implementation of the time-delay RC, where the nonlinearity was provided by a Mach-Zehnder modulator (MZM). Duport et al. [17] proposed a time-delay RC scheme, using the saturation of a semiconductor optical amplifier as nonlinearity. Brunner et al. [18] experimentally realized the time-delay RC by utilizing the transient response of the single-mode semiconductor laser (SL) with optical feedback. Nguimdo et al. [22] proposed a time-delay RC by adopting a single quantum cascade laser with optical feedback, and the input signal was injected directly in the feedback loop. It was proved that such RC system was robust to feedback phase. Sugano et al. [23] put forward a scheme for RC employed multiple SLs with optical feedbacks. The SLs were arrayed on a photonic integrated circuit in parallel.

Because of the advantages of low manufacturing cost, energy-efficiency, easy to integrate to two-dimensional arrays and rich polarization dynamics [24, 25], using vertical-cavity surface-emitting laser (VCSEL) as the nonlinear node for the time-delay RC has also attracted a lot of attentions [26–29]. For instance, an enhanced RC performance by adopting the polarization dynamics in VCSEL was demonstrated for the first time by Vatin et al. [26]. Besides, in our previous studies, two independent tasks were processed simultaneously by employing two polarization-resolved modes in a VCSEL-based RC system [29]. Four-channels RC system was achieved by utilizing mutually coupled VCSELs [28]. Compared with one-channel RC system, comparable RC performance with four times faster information processing rate can be obtained by using such four-channels RC system.

It is well known that memory capacity (MC) is one of the essential properties for processing temporal sequence for RC [30–32]. In a recurrent neural network, memory is derived from the recurrent network connections, which allows information to remain in the network for a limited time [30]. As a result, past information is mixed with current input. In the photon recurrent neural network, recurrences are introduced by optical delay feedback, thus forming a ring topology [31]. In other words, MC is the property of a system to keep the previous input information. In an RC system, the reservoir states are affected by the short-term inputs, but independent of the long-term inputs [14]. For instance, for the speech recognition task, only the recent signal is important [14]. Currently, most of the studies have focused on the MC of time-delay RC systems with single optical feedback (SOF). To our knowledge, related investigations have demonstrated that the performance of RC can benefit from more than one optical feedback [33]. However, the MC of the time-delay RC based on a VCSEL with double optical feedbacks (DOF) has not yet been explored.

In this paper, we propose a time-delay RC based on a VCSEL with DOF. The MC of the proposed system is investigated in detail. For the purpose of comparison, the VCSEL-based RC system with SOF is also considered. The rest of this paper is organized as follows. In Section 2, the system model of the VCSEL-based RC system with DOF, the rate equation model of response VCSEL, and the MC are introduced in detail. In Section 3, the numerical analysis of MC has been performed and compared for both the VCSEL-based RC systems with SOF and DOF. The effects of the feedback strength, injection strength, frequency detuning, injection current, and feedback delays are also analyzed in detail. Besides, the corresponding parameter regions leading to higher MC are further identified. Finally, the conclusion is given in Section 4.

2   Theory and model

The schematic diagram of the VCSEL-based RC system with DOF is shown in Figure 1. Note that, there are X-polarization (XP) and Y-polarization (YP) modes in VCSEL for some specific situations [34,35]. In this system, a VCSEL subject to DOF is regarded as a reservoir. The output of the VCSEL is divided into two parts, which are re-injected into the VCSEL. Two variable optical attenuators (VOA1 and VOA2) are employed to adjust the feedback strengths of the two parts, respectively. Different feedback delays can be obtained by adjusting the fiber delay lines (DL1 and DL2). An input signal $u(k)$ after being masked is injected to the XP mode of the VCSEL through an MZM [36]. An SL is used as a driver for
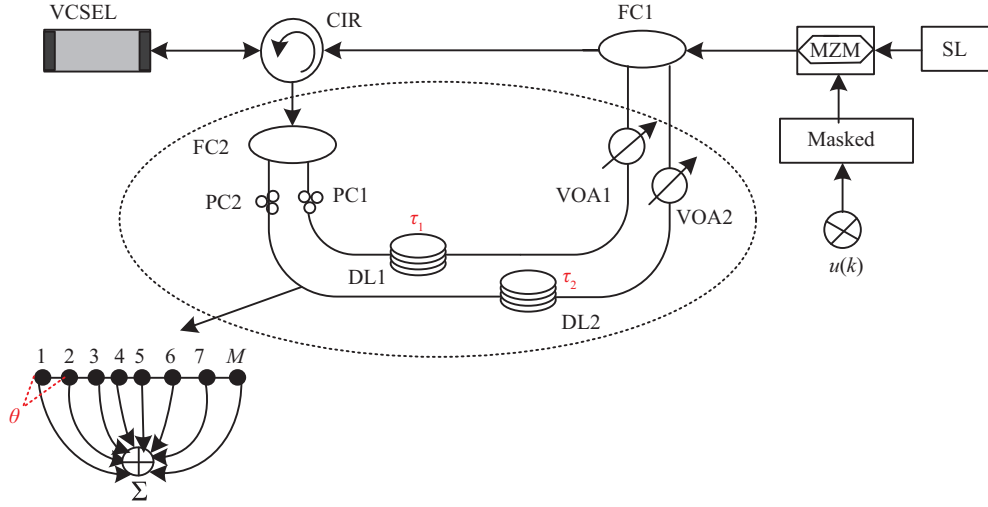
Figure 1 (Color online) Schematic diagram of the VCSEL-based RC system with DOF. MZM: Mach-Zehnder modulator; PC1 (PC2): polarization controller; VOA1 (VOA2): variable optical attenuator; DL1 (DL2): fiber delay line; CIR: optical circulator; FC1 (FC2): fiber coupler; SL: semiconductor laser; $u(k)$: input data.

the MZM. Here, in our system, a random mask with two discrete levels $(1, -1)$ is employed [37]. The amplitude of the masked input signal $(s(t))$ is rescaled, and $-1 < s(t) < 1$. The mask process, which is acted as weights multiplied on the input signal, is similar to [15]. The sample-and-hold time of the mask process is set to T, and an input data is injected to the reservoir for each T. Thus, the information processing rate is the reciprocal of T. The value of mask is changed for each interval θ between two adjacent virtual nodes. The virtual nodes is represented as M. θ should be smaller than the relaxation oscillation period of the VCSEL for complex transient response [15]. The feedback delays are set to be τ_1 and τ_2, respectively. Note that, we only fix $\tau_1 = T = M \times \theta$. In the output layer, the transient states of the virtual nodes of the RC system are extracted. Then the optimal output weights are determined during the training process by minimizing the normalized mean square error of the predicted values to the same target values.

The dynamics of the response VCSEL subject to DOF is modeled by the well-known spin-flip model [38–43]. Here, we only consider the parallelly-polarized optical feedback. The rate equations are described as

$$
\begin{aligned}
\frac{\mathrm{d}E_x}{\mathrm{d}t} =& \kappa(1 + \mathrm{i}\alpha)(NE_x - E_x + \mathrm{i}nE_y) - (\gamma_a + \mathrm{i}\gamma_p)E_x + k_{d1x}E_x(t - \tau_1)\mathrm{e}^{-\mathrm{i}\omega_x\tau_1} \\
& + k_{d2x}E_x(t - \tau_2)\mathrm{e}^{-\mathrm{i}\omega_x\tau_2} + k_{\mathrm{inj}}\epsilon(t) + F_x(t),
\end{aligned}
\tag{1}
$$

$$
\begin{aligned}
\frac{\mathrm{d}E_y}{\mathrm{d}t} =& \kappa(1 + \mathrm{i}\alpha)(NE_y - E_y - \mathrm{i}nE_x) + (\gamma_a + \mathrm{i}\gamma_p)E_y + k_{d1y}E_y(t - \tau_1)\mathrm{e}^{-\mathrm{i}\omega_y\tau_1} \\
& + k_{d2y}E_y(t - \tau_2)\mathrm{e}^{-\mathrm{i}\omega_y\tau_2} + F_y(t),
\end{aligned}
\tag{2}
$$

$$
\frac{\mathrm{d}N}{\mathrm{d}t} = \gamma_N[\mu - N(1 + |E_x|^2 + |E_y|^2) + \mathrm{i}n(E_xE_y^* - E_yE_x^*)],
\tag{3}
$$

$$
\frac{\mathrm{d}n}{\mathrm{d}t} = -\gamma_s n - \gamma_N[n(|E_x|^2 + |E_y|^2) + \mathrm{i}N(E_yE_x^* - E_xE_y^*)],
\tag{4}
$$

$$
\epsilon(t) = \frac{1}{2}|\epsilon_0|(1 + \mathrm{e}^{\mathrm{i}[s(t)+\Phi_0]})\mathrm{e}^{\mathrm{i}2\pi\Delta ft},
\tag{5}
$$

where E_x (E_y) represents the slowly varied complex field amplitudes of the XP (YP) mode. N stands for the total carrier inversion between conduction and valence bands, while n accounts for the difference between carrier inversions with opposite spins. The third term and fourth term in (1) and (2) stand for the DOF. The feedback strengths are k_{d1x}, k_{d2x}, k_{d1y} and k_{d2y}. The injection from MZM is represented by $k_{\mathrm{inj}}\epsilon(t)$ in the fifth term of (1), where k_{inj} means the injection strength. Besides, α is the linewidth enhancement factor, κ is the field decay rate, γ_N is the decay rate of N, γ_s is the spin-flip rate, γ_a (γ_p)

represents the linear dichroism (the linear birefringence). μ is the normalized injection current, while $\mu = 1$ implies at the threshold. $\omega_x = \omega_0 + \kappa\gamma_a - \gamma_p$ ($\omega_0 = 2\pi c\lambda$) is the angular frequency of the XP mode, and $\omega_y = \omega_0 + \gamma_p - \kappa\gamma_a$ denotes the angular frequency of the YP mode. The external injection is represented by $\epsilon(t)$ in (5). $|\epsilon_0|$ (ϕ_0) represents the injection field amplitude (bias voltage of the MZM). The frequency detuning between the XP mode of VCSEL and the injected field is represented as Δf. Modeled by the Langevin sources, the spontaneous emission noise in the last terms of (1) and (2) is denoted as [28] $F_x = \sqrt{\frac{\beta}{2}}(\sqrt{N+n}\xi^a + \sqrt{N-n}\xi^b)$ and $F_y = -\mathrm{i}\sqrt{\frac{\beta}{2}}(\sqrt{N+n}\xi^a - \sqrt{N-n}\xi^b)$. β is the strength of the spontaneous emission. ξ^a and ξ^b are the independent Gaussian white noises source with unit variance and zero mean. We numerically solve (1)–(5) by the second-order Runge-Kutta method adopting an integration step of 2 ps with typical parameters for 850 nm VCSEL [28]: $\kappa = 300$ ns^{-1}, $\alpha = 3$, $\gamma_a = 0.1$ ns^{-1}, $\gamma_s = 50$ ns^{-1}, $\gamma_p = 10$ ns^{-1}, $\gamma_N = 1$ ns^{-1}, $\beta = 10^{-6}$. Besides, we consider $M = 100$, $\theta = 10$ ps, $\tau_1 = T = M \times \theta = 1$ ns (the information processing rate of the RC system is 1 Gpbs), $\tau_2 = 3.1$ ns, $|\epsilon_0| = 2$, $\Phi_0 = 0$ [19]. Note, the parameters mentioned above are fixed, unless otherwise indicated.

Here, we adopt a method introduced in [20] to measure the MC of the VCSEL-based RC system with DOF. A pseudo-random numbers $u(k)$ between 0 and 1 is used as input. In this study, 800 points of $u(k)$ are used for training and the next 200 points are adopted for verification [20]. The j-delay MC (mc$_j$) represents the correlation between the current output $y(k)$ and the input $u(k-1)$ of j time steps before, which is described as [44]

$$\mathrm{mc}_j = \frac{\mathrm{Cov}^2(u(k-j), y(k))}{\mathrm{Var}(u(k))\mathrm{Var}(y(k))}, \tag{6}$$

where Cov is covariance, and Var denotes variance. The value of mc$_j = 1$ stands for that the RC system perfectly retains information about the past input data of j time-steps ago. mc$_j$ is also called linear memory. Then all accumulated mc$_j$ is regarded as the MC, which is denoted as [44]

$$\mathrm{MC} = \sum_{j=1}^{i} \mathrm{mc}_j. \tag{7}$$

3 Numerical results and discussion

In this section, the MC of the VCSEL-based RC system with DOF is investigated numerically. For the purpose of comparison, we also consider the VCSEL-based RC system with SOF. The influences of feedback strength, injection strength, injection current, as well as frequency detuning are examined carefully. Moreover, the influence of feedback delays is also taken into account.

At first, the polarization-resolved intensities of the VCSEL as a function of the injection current are shown in Figure 2. The mean output intensity is denoted as $\langle I_x \rangle = \langle |E_x(t)|^2 \rangle$ ($\langle I_y \rangle = \langle |E_y(t)|^2 \rangle$) for the XP (YP) mode. Here, we fix $k_{\mathrm{inj}} = 0$ ns^{-1}. On one hand, as can be seen from Figure 2(a), for $k_{d1x} = k_{d2x} = k_{d1y} = k_{d2y} = 0$, when $1 < \mu < 2.6$, the XP mode is the dominant polarization mode, and the YP mode is suppressed. Until $\mu = 2.6$, the polarization switching (PS) appears. With the further growth of μ, the YP mode becomes the dominant polarization mode and the XP mode is suppressed. On the other hand, for $k_{d1x} = k_{d2x} = k_{d1y} = k_{d2y} = 10$ ns^{-1}, similar results can be observed, and the PS appears in $\mu = 3.5$. In this study, we choose $\mu = 1.2$, in which the YP mode is almost suppressed. Thus, we ignore the feedback terms in YP mode, and the transient response is only calculated as $\langle I_x \rangle = \langle |E_x(t)|^2 \rangle$. Moreover, we have also considered the time-varying injection current, i.e., increasing firstly and then decreasing. It is found that, the bistability is only observed in small μ. However, when external injection and self-feedback are added, the bistability cannot be observed.

Then the values of MC of the VCSEL-based RC system with SOF and DOF are compared. For clarity, the total feedback strength is denoted as $k_{ds} = k_{d1x}$ for the VCSEL-based RC system with SOF, and is denoted as $k_{ds} = k_{d1x} + k_{d2x}$ for the VCSEL-based RC system with DOF. For direct comparison, identical
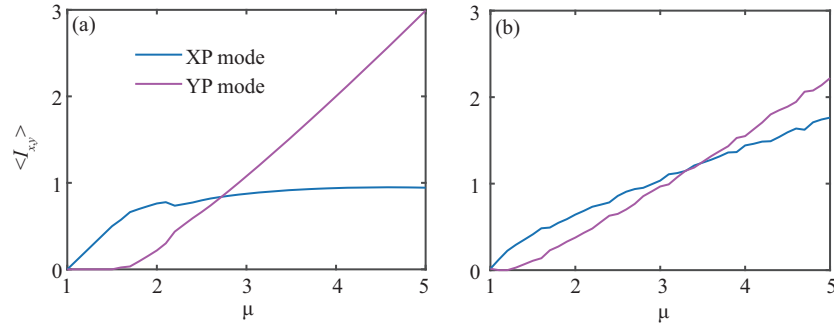
Figure 2 (Color online) The polarization-resolved intensities as a function of the injection current μ for XP and YP modes of the VCSEL, for (a) $k_{d1x} = k_{d2x} = k_{d1y} = k_{d2y} = 0$, (b) $k_{d1x} = k_{d2x} = k_{d1y} = k_{d2y} = 10$ ns^{-1}, with $k_{\rm inj} = 0$, $\tau_1 = 1$ ns, $\tau_2 = 3.1$ ns, $\Delta f = 0$ GHz.
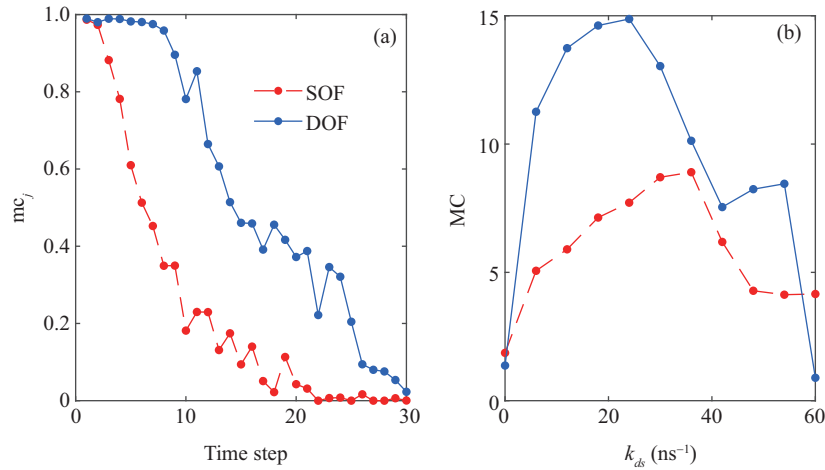
Figure 3 (Color online) (a) The j-delay memory capacity mc$_j$ with $k_{ds} = 20$ ns^{-1} for both systems; (b) memory capacity MC as a function of the feedback strength k_{ds} when j is set to be 30, with $k_{\rm inj} = 20$ ns^{-1}, $\tau_1 = 1$ ns, $\tau_2 = 3.1$ ns, $\mu = 1.2$, $\Delta f = 0$ GHz for the VCSEL-based RC with DOF and SOF.

k_{ds} is adopted for the both systems. Here, we consider $k_{d1x} = k_{d2x} = 10$ ns^{-1}, $\tau_1 = 1$ ns, $\tau_2 = 3.1$ ns for the VCSEL-based RC system with DOF, and $k_{ds} = 20$ ns^{-1}, $\tau_1 = 1$ ns for the VCSEL-based RC system with SOF. The mc$_j$ is shown in Figure 3(a). Here, $k_{\rm inj} = 20$ ns^{-1} is fixed for both cases. It can be seen that, for the VCSEL-based RC system with DOF, the values of mc$_j$ start to decrease when $j > 4$. While, the values of mc$_j$ start to decrease when $j > 1$ for the VCSEL-based RC system with SOF. In addition, the VCSEL-based RC system with DOF can remember almost 96% of the information injected 7 time-steps ago. While for the VCSEL-based RC system with SOF, only 45% of the information injected 7 time-steps ago can be remembered. It is obvious that the values of mc$_j$ for the VCSEL-based RC system with DOF is larger than those for the VCSEL-based RC system with SOF. Besides, for both RC systems, the information injected 30 time-steps ago approaches 0. Thus, j is fixed at 30 for the following part.

For further comparison of both RC systems, the values of MC as a function of the total feedback strength k_{ds} are shown in Figure 3(b). For the VCSEL-based RC system with SOF, k_{d1x} is varied from 0 to 60 ns^{-1}. For the VCSEL-based RC system with DOF, we set $k_{d1x} = k_{d2x}$, k_{d1x} and k_{d2x} are varied from 0 to 30 ns^{-1}. It can be seen that, the values of MC increase linearly with k_{ds} when $0 < k_{ds} < 24$ ns^{-1} $(0 < k_{ds} < 36$ ns$^{-1})$ for the VCSEL-based RC system with DOF (with SOF), then decrease with the further increase of k_{ds} in general. The highest MC value can reach 15 for the VCSEL-based RC system with DOF, which is larger than the MC value obtained in [20, 26]. Obviously, the values of MC for the VCSEL-based RC system with DOF are higher than those for the VCSEL-based RC system with SOF. That is to say, compared to the VCSEL-based RC system with SOF, a enhanced MC can be obtained
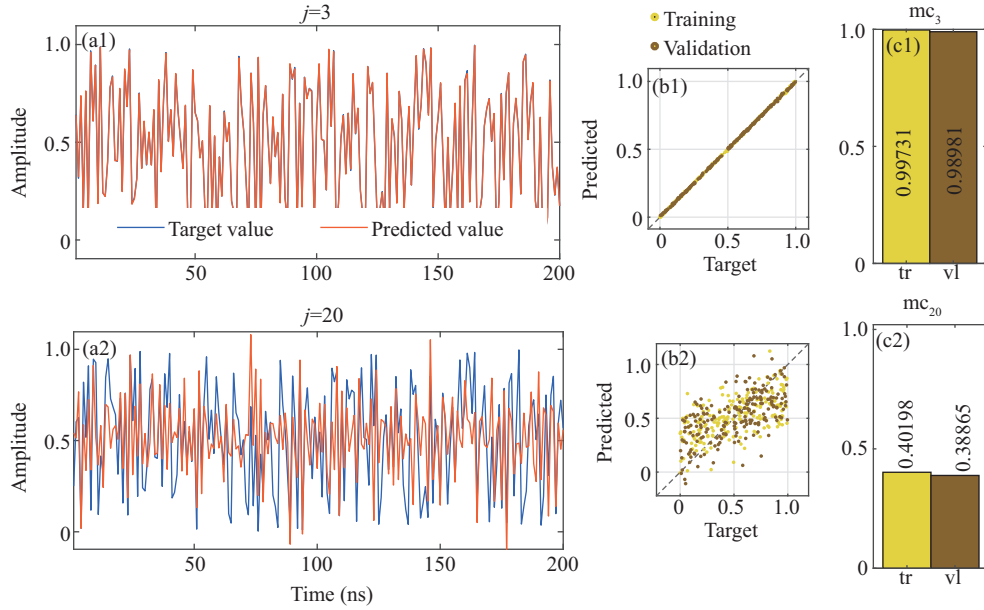
Figure 4 (Color online) (a1) and (a2) Comparison between the target values (blue) and predicted values (orange) for $j = 3$ (top) and for $j = 20$ (bottom). (b1) and (b2) Scatter plots of the target values verses predicted values. (c1) and (c2) the MC values for training (brown) and validation data sets (yellow).

for the VCSEL-based RC system with DOF in a wide feedback strength range. That is may be more rich dynamic that can be introduced to the RC system by more feedbacks [45, 46]. Note, we have also considered the case of a larger injection current, and found that higher MC can also be obtained, as long as the $k_{\rm inj}$ is appropriately increased.

Meanwhile, a closer look of the MC for the VCSEL-based RC system with DOF is shown in Figure 4. On one hand, the case of $j = 3$ is presented in Figure 4(a1)–(c1). As can be seen from Figure 4(a1), it is obvious that the time series for the predicted values are fairly close to the target values. Scatter plots of the predicted values verse the target values are almost coincided as can be seen from Figure 4(b1) for training and validation phases, respectively. Beside, as shown in Figure 4(c1), we also give the MC values for the training (MC = 0.99731) and verification (MC = 0.98981) phases, respectively. On the other hand, for the case of $j = 20$, as shown in Figure 4(a2)–(c2), the mismatch between the predicted values and the target values is obvious. The MC values for the training and verification phase are 0.40198 and 0.38865, respectively.

In the following, we only focus on the VCSEL-based RC system with DOF. To obtain the dependence of MC, the two dimensional maps of MC in the parameter space of feedback strengths k_{d1x} and k_{d2x} for $k_{\rm inj} = 20$ ns^{-1} and $k_{\rm inj} = 30$ ns^{-1} are shown in Figure 5. Here, we consider $\mu = 1.2$. To better distinguish the regions of MC in Figures 5(a) and (b), the parameter space is divided into region A corresponding to MC $\geqslant 14$ and region B contributing to MC $\geqslant 18$. On one hand, for $k_{\rm inj} = 20$ ns^{-1}, it can be seen from Figure 5(a), the region A is almost located at the region of $0 < k_{d1x} < 18$ ns^{-1} and 6 ns$^{-1} < k_{d2x} < 22$ ns^{-1}. For a given k_{d2x}, the MC values increase first with k_{d1x}, then decrease with the further growth of k_{d1x}. In addition, region B is almost located at the central area of region A. It is verified that, smaller k_{d1x} and moderate k_{d2x} are desired to obtain enhanced MC. On the other hand, as can be seen from Figure 5(b), for $k_{\rm inj} = 30$ ns^{-1}, similar trend can be observed and both regions A and B are wider than those for $k_{\rm inj} = 20$ ns^{-1}. Besides, the highest MC value is 23. It is proved again that enhance MC can be achieved for the VCSEL-based RC system with DOF.

Subsequently, two dimensional map of the values of MC in the parameter space of injection strength and feedback strength is shown in Figure 6. On one hand, as can be seen from Figure 6(a), for $k_{d1x} = k_{d2x}$, the contour line MC = 20 (MC = 14) divides the parameter space into region A (B) corresponding to MC $\geqslant 20$ (MC $\geqslant 14$). It can be seen that, when $k_{\rm inj} \geqslant 20$ ns^{-1}, the region B basically occupies the
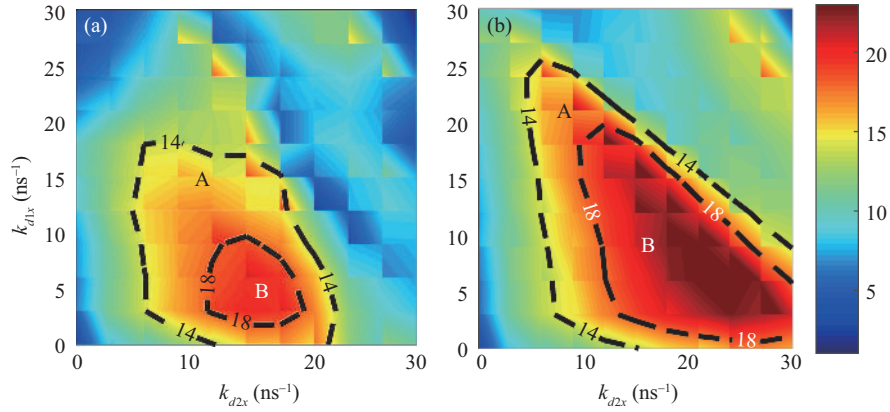
Figure 5 (Color online) Two dimensional map of the values of MC in the parameter space of k_{d1x} and k_{d2x}, for (a) $k_{inj} = 20$ ns^{-1}, (b) $k_{inj} = 30$ ns^{-1}, with $\tau_1 = 1$ ns, $\tau_2 = 3.1$ ns, $\mu = 1.2$, $\Delta f = 0$ GHz for the VCSEL-based RC with DOF.
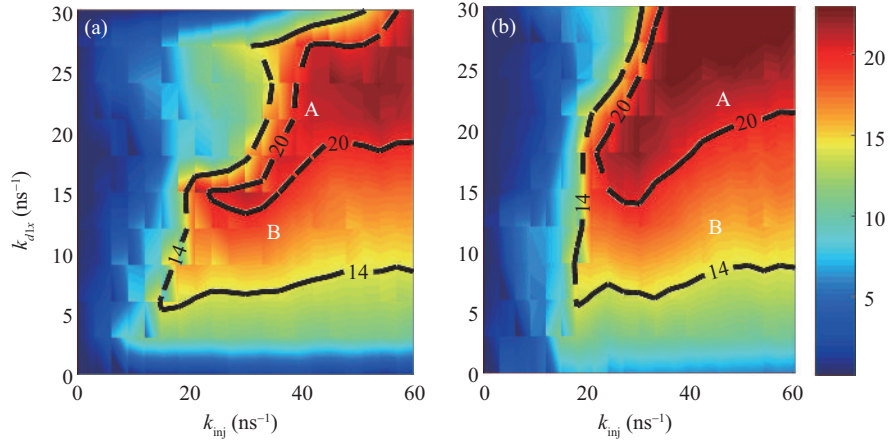

Figure 6 (Color online) Two dimensional map of the values of MC in the parameter space of k_{inj} and k_{d1x}, for (a) $k_{d1x} = k_{d2x}$, (b) $k_{d1x} = 10$ ns^{-1}, with $\tau_1 = 1$ ns, $\tau_2 = 3.1$ ns, $\mu = 1.2$, $\Delta f = 0$ GHz for the VCSEL-based RC with DOF.

diagonal area. As k_{d1x} is increased, MC increases first and then decreases for a given k_{inj}. Moreover, for a larger k_{inj}, region B spans a wider range of k_{d1x}. Besides, region A is almost in the upper half of region B. On the other hand, for $k_{d1x} = 10$ ns^{-1}, similar results can be also obtained. That is to say, a larger k_{inj} is desired to obtain higher MC values in a wider range of feedback strength, which is owing to the injection locking effect [20].

Then, the influence of frequency detuning Δf is also take into account. Two-dimensional maps of MC values in the parameter space of external injection strength k_{inj} and frequency detuning Δf are presented for different k_{d1x} and k_{d2x} in Figure 7. Here, the total feedback strength k_{ds} is fixed at 20 ns^{-1} for the three considered cases. A higher MC region with MC $\geqslant 12$ is regarded as region A by the contour lines. On one hand, as shown in Figure 7(a), for $k_{d1x} = 5$ ns^{-1} and $k_{d2x} = 15$ ns^{-1}, the region A mainly locates at larger k_{inj} and negative Δf, which is consistent with the injection locking area obtained in [47,48]. The higher values of MC in region A occupy near $\Delta f = 0$ GHz. On the other hand, for other two cases of $k_{d1x} = 10$ ns^{-1} and $k_{d2x} = 10$ ns^{-1}, $k_{d1x} = 12$ ns^{-1} and $k_{d2x} = 8$ ns^{-1} in Figures 7(b) and (c), similar results can be also obtained. It is indicated that larger k_{inj} and negative Δf or Δf around 0 is more easy to lead a higher MC.

Next, the values of MC as a function of bias current for different external injection strength are further shown in Figure 8. Here $k_{d1x} = k_{d2x} = 10$ ns^{-1}, $\tau_1 = 1$ ns, $\tau_2 = 3.1$ ns are fixed. As can be seen that, for $k_{inj} = 20$ ns^{-1}, MC is approximately 17 when $\mu \leqslant 1.2$. For higher bias current μ, because of the onset of
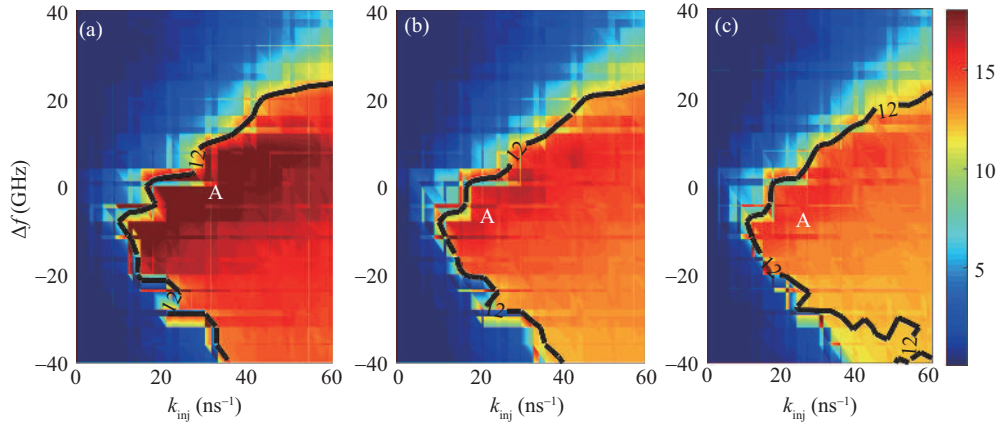
Figure 7 (Color online) Two dimensional map of the values of MC in the parameter space of k_{inj} and Δf, with $\tau_1 = 1$ ns, $\tau_2 = 3.1$ ns, $\mu = 1.2$, for (a) $k_{d1x} = 5$ ns^{-1} and $k_{d2x} = 15$ ns^{-1}, (b) $k_{d1x} = 10$ ns^{-1} and $k_{d2x} = 10$ ns^{-1}, (c) $k_{d1x} = 12$ ns^{-1} and $k_{d2x} = 8$ ns^{-1} for the VCSEL-based RC with DOF.
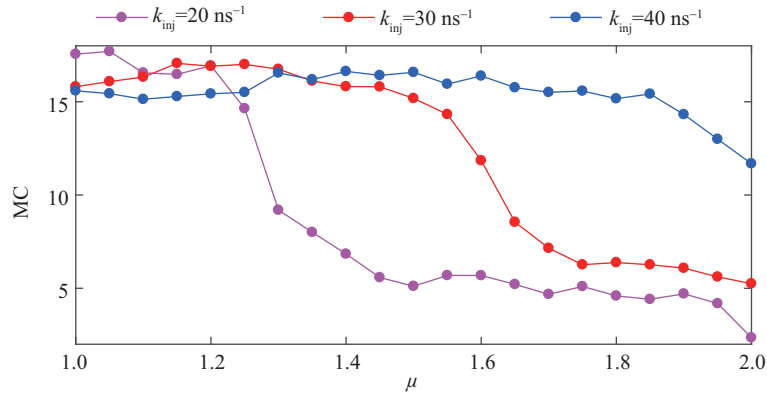

Figure 8 (Color online) The MC values as a function of μ for $k_{\mathrm{inj}} = 20$ ns^{-1}, $k_{\mathrm{inj}} = 30$ ns^{-1} and $k_{\mathrm{inj}} = 40$ ns^{-1}, with $k_{d1x} = k_{d2x} = 10$ ns^{-1}, with $\tau_1 = 1$ ns, $\tau_2 = 3.1$ ns, $\Delta f = 0$ GHz for the VCSEL-based RC with DOF.

delayed feedback instabilities, MC decreases significantly. It is indicated that the highest MC is obtained for μ close to VCSEL threshold, which agrees well with the results of chaotic time series prediction task in [37]. Moreover, for a larger k_{inj}, such as $k_{\mathrm{inj}} = 30$ ns^{-1} and $k_{\mathrm{inj}} = 40$ ns^{-1}, similar trends can also be observed. For $k_{\mathrm{inj}} = 30$ ns^{-1} ($k_{\mathrm{inj}} = 40$ ns^{-1}), the curve of MC fluctuates around MC $= 16$ (MC $= 15.5$) when $\mu \leqslant 1.5$ ($\mu \leqslant 1.9$), then the values of MC decrease significantly with the further growth of μ. That is to say, a wider range of delayed feedback stabilities can be achieved by a larger k_{inj}. However, for all the cases, before the onset of delayed feedback instabilities, a larger k_{inj} leads to a slightly lower values of MC.

At last, we also consider the effect of feedback delays on the MC values of the VCSEL-based RC system with DOF. Here, $\tau_1 = T = 1$ ns is fixed, only the feedback delay τ_2 is changed. The values of MC as a function of feedback delay τ_2 are shown in Figure 9. On one hand, for $k_{\mathrm{inj}} = 30$ ns^{-1}, the values of MC generally increase with τ_2 for 0.5 ns $< \tau_2 < 6.6$ ns, then decrease when 6.6 ns $< \tau_2 < 15.2$ ns for all the given k_{d1x} and k_{d2x}. However, there are several special points corresponding to lower values of MC, such as, point "a" ($\tau_2 = 5\tau_1$), point "b" ($\tau_2 = 6.5\tau_1$), point "c" ($\tau_2 = 8\tau_1$), and point "d" ($\tau_2 = 9\tau_1$). Note that, these special combinations of time delays have also been identified experimentally and numerically, which lead to lower time delay signature concealment performance and lower complexity in SL with DOF [45, 46]. Moreover, for $k_{\mathrm{inj}} = 40$ ns^{-1}, similar results are observed in Figure 9(b). Hence, this dependence can be regarded as a suggested rule for selecting the feedback delays to obtain the higher MC in the VCSEL-based RC system with DOF.

In order to analyze the special cases mentioned in Figure 9 more intuitively, the variation of MC values
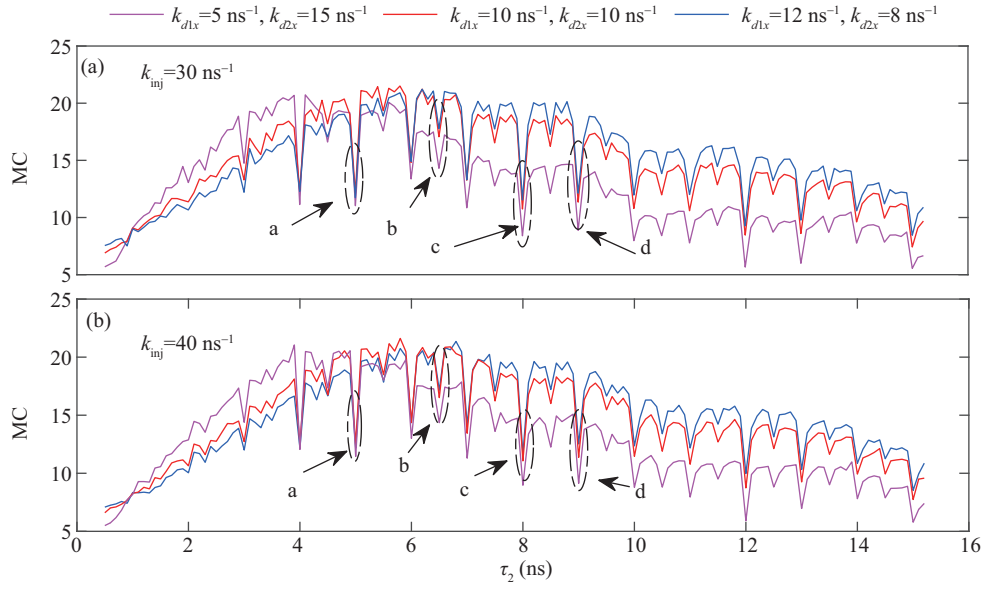
Figure 9 (Color online) The MC values as a function of τ_2 for (a) $k_{\mathrm{inj}} = 30$ ns^{-1} and (b) $k_{\mathrm{inj}} = 40$ ns^{-1}, point "a" ($\tau_2 = 5$ ns), point "b" ($\tau_2 = 6.5$ ns), point "c" ($\tau_2 = 8$ ns), and point "d" ($\tau_2 = 9$ ns), with $k_{d1x} = 5$ ns^{-1} and $k_{d2x} = 15$ ns^{-1}, $k_{d1x} = 10$ ns^{-1} and $k_{d2x} = 10$ ns^{-1}, $k_{d1x} = 12$ ns^{-1} and $k_{d2x} = 8$ ns^{-1}, $\tau_1 = 1$ ns, $\Delta f = 0$ GHz for the VCSEL-based RC with DOF.
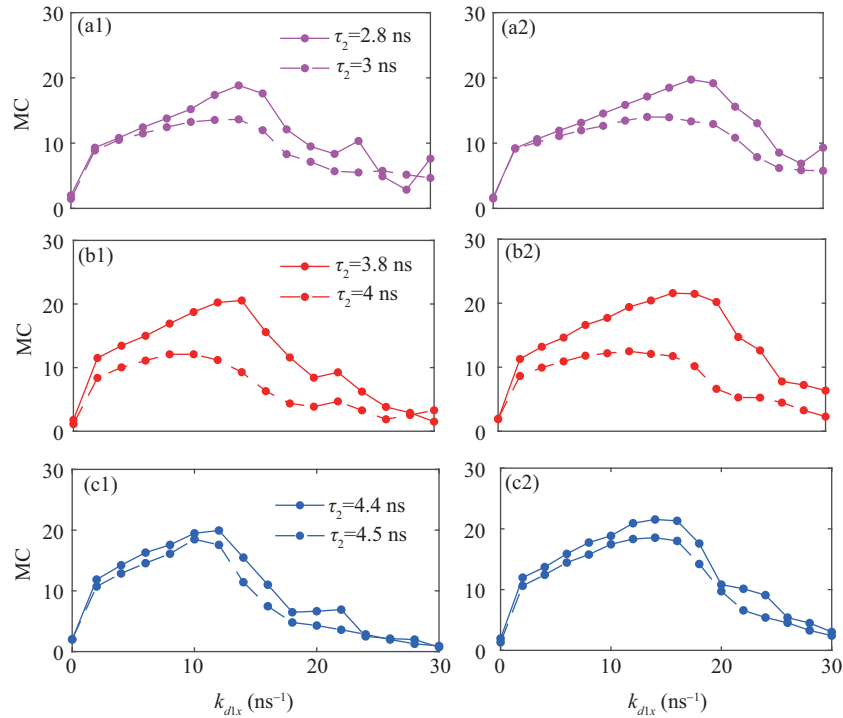

Figure 10 (Color online) The MC values as a function of k_{d1x} for (a1) $\tau_2 = 2.8$ ns^{-1} and (a2) $\tau_2 = 3$ ns^{-1}, (b1) $\tau_2 = 3.8$ ns^{-1} and (b2) $\tau_2 = 4$ ns^{-1}, (c1) $\tau_2 = 4.4$ ns^{-1} and (c2) $\tau_2 = 4.5$ ns^{-1}, with (a1)–(c1) $k_{\mathrm{inj}} = 30$ ns^{-1}, and (a2)–(c2) $k_{\mathrm{inj}} = 40$ ns^{-1}, with $k_{d1x} = k_{d2x}$, $\tau_1 = 1$ ns, $\Delta f = 0$ GHz for the VCSEL-based RC with DOF.

with feedback strength is further shown in Figure 10. Note that $k_{d1x} = k_{d2x}$ is fixed. Here, we consider three combinations of feedback delays ($\tau_2 = 2.8\tau_1$ and $\tau_2 = 3\tau_1$, $\tau_2 = 3.8\tau_1$ and $\tau_2 = 4\tau_1$, $\tau_2 = 4.4\tau_1$ and $\tau_2 = 4.5\tau_1$), and the information processing time T is set equal to be τ_1. Obviously, when two feedback delays are $\frac{1}{2}$ multiples ($\frac{\tau_2}{\tau_1} = \frac{1}{2}L$, L is the integer), lower MC values would be observed.
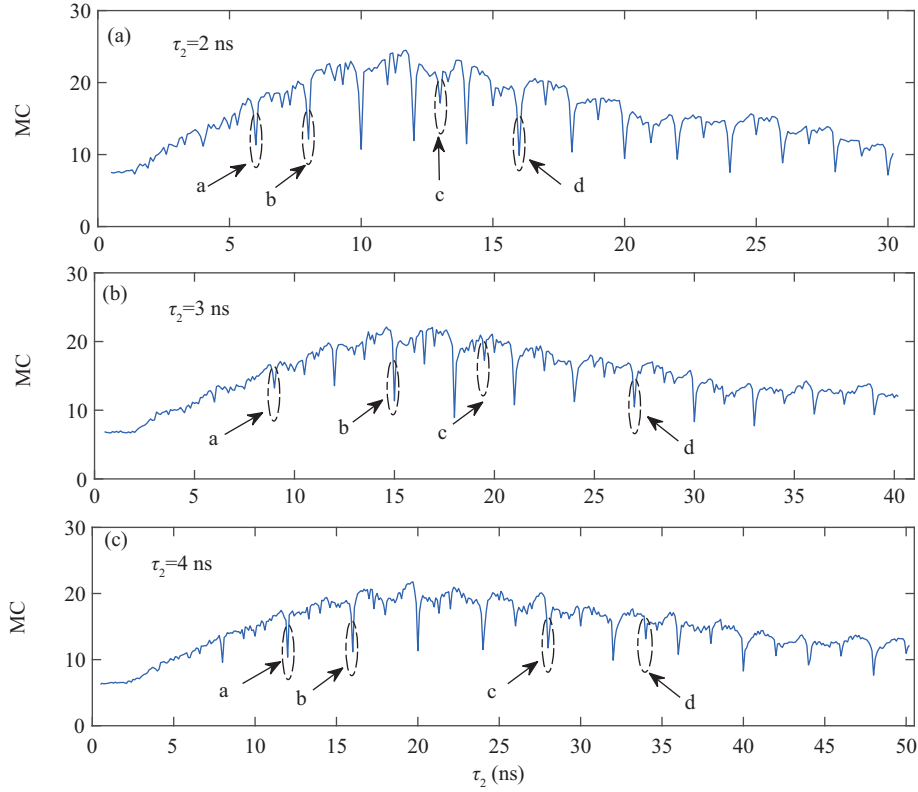
Figure 11 (Color online) The MC values as a function of τ_2 for (a) $\tau_1 = 2$ ns^{-1}, point "a" ($\tau_2 = 3\tau_1 = 6$ ns), point "b" ($\tau_2 = 4\tau_1 = 8$ ns), point "c" ($\tau_2 = 6.5\tau_1 = 13$ ns), and point "d" ($\tau_2 = 8\tau_1 = 16$ ns); (b) $\tau_1 = 3$ ns^{-1}, point "a" ($\tau_2 = 3\tau_1 = 9$ ns), point "b" ($\tau_2 = 5\tau_1 = 15$ ns), point "c" ($\tau_2 = 6.5\tau_1 = 19.5$ ns), and point "d" ($\tau_2 = 9\tau_1 = 27$ ns); (c) $\tau_1 = 4$ ns^{-1}, point "a" ($\tau_2 = 3\tau_1 = 12$ ns), point "b" ($\tau_2 = 4\tau_1 = 16$ ns), point "c" ($\tau_2 = 7\tau_1 = 28$ ns), and point "d" ($\tau_2 = 8.5\tau_1 = 34$ ns) with $k_{\text{inj}} = 30$ ns^{-1}, $k_{d1x} = k_{d2x} = 10$ ns^{-1}, $\Delta f = 0$ GHz for the VCSEL-based RC with DOF.

In the above part, we only focus on the case of $\tau_1 = T = 1$ ns. Without loss of generality, we also considerate some larger feedback delays τ_1. Here, we only consider $k_{\text{inj}} = 30$ ns^{-1}. On one hand, as can be seen from Figure 11(a), for $\tau_1 = T = 2$ ns, similar trends to $\tau_1 = T = 1$ ns can be obtained. The MC values generally present increasing firstly and then decreasing trend with the increase of τ_2. Besides, some special points also can be observed, such as point "a" ($\tau_2 = 3\tau_1 = 6$ ns), point "b" ($\tau_2 = 4\tau_1 = 8$ ns), point "c" ($\tau_2 = 6.5\tau_1 = 13$ ns), and point "d" ($\tau_2 = 8\tau_1 = 16$ ns). The highest MC value is 24.5 obtained at $\tau_2 = 11.7$ ns which is larger than that for the case of $\tau_1 = T = 1$ ns (in the case of $\tau_1 = T = 1$ ns, the highest value MC = 21.2 is observed at $\tau_2 = 6.6$ ns). On the other hand, for even larger τ_1, such as $\tau_1 = T = 3$ ns, $\tau_1 = T = 4$ ns, as shown in Figures 11(b) and (c), similar results can also be obtained. For $\tau_1 = T = 3$ ns ($\tau_1 = T = 4$ ns), the highest MC value is 21.5 (21.67) obtained at $\tau_2 = 17.4$ ns ($\tau_2 = 19.6$ ns). That is to say, a higher τ_1 can lead to a wider region of better MC. Moreover, we have also considered a case of $\tau_1 = T = 10$ ns (not shown here), and found that similar results can also be obtained.

4　Conclusion

In summary, we mainly numerically investigate the enhanced memory capacity of the time-delay RC based on a VCSEL with DOF. It is found that, the VCSEL-based RC system with DOF can produce higher memory capacity compared with the VCSEL-based RC system with SOF. Besides, numerical simulation results show that feedback strength, injected strength, frequency detuning as well as injection current are suggested as the key factors to obtain enhanced memory capacity of the VCSEL-based RC system with DOF. More precisely, the parameter regions leading to higher memory capacity are greatly broadened for

moderate values of feedback strength, larger injection strength, lower bias current or negative frequency detuning. In addition, when two feedback delays are $\frac{1}{2}$ multiples, the memory capacity is much lower. Moreover, we find that a larger feedback delay or information processing time can lead to a wider region of higher memory capacity.

References

1 Maass W, Natschläger T, Markram H. Real-time computing without stable states: a new framework for neural computation based on perturbations. Neural Comput, 2002, 14: 2531–2560
2 Jaeger H, Haas H. Harnessing nonlinearity: predicting chaotic systems and saving energy in wireless communication. Science, 2004, 304: 78–80
3 Verstraeten D, Schrauwen B, Stroobandt D, et al. Isolated word recognition with the liquid state machine: a case study. Inf Process Lett, 2005, 95: 521–528
4 Verstraeten D, Schrauwen B, Stroobandt D. Reservoir-based techniques for speech recognition. In: Proceedings of International Joint Conference on Neural Networks, 2006. 1050–1053
5 Martinenghi R, Rybalko S, Jacquot M, et al. Photonic nonlinear transient computing with multiple-delay wavelength dynamics. Phys Rev Lett, 2012, 108: 244101
6 Vinckier Q, Duport F, Smerieri A, et al. High-performance photonic reservoir computer based on a coherently driven passive cavity. Optica, 2015, 2: 438–446
7 Argyris A, Bueno J, Fischer I. PAM-4 transmission at 1550 nm using photonic reservoir computing post-processing. IEEE Access, 2019, 7: 37017–37025
8 Yue D Z, Wu Z M, Hou Y S, et al. Performance optimization research of reservoir computing system based on an optical feedback semiconductor laser under electrical information injection. Opt Express, 2019, 27: 19931
9 Jalalvand A, Vandersmissen B, Neve W De, et al. Radar signal processing for human identification by means of reservoir computing networks. In: Proceedings of IEEE Radar Conference (RadarConf19), 2019. 1–6
10 Antonik P, Marsal N, Rontani D. Large-scale spatiotemporal photonic reservoir computer for image classification. IEEE J Sel Top Quantum Electron, 2020, 26: 1–12
11 Jüngling T, Lymburn T, Stemler T, et al. Reconstruction of complex dynamical systems from time series using reservoir computing. In: Proceedings of IEEE International Symposium on Circuits and Systems (ISCAS), 2019. 1–5
12 Pathak J, Hunt B, Girvan M, et al. Model-free prediction of large spatiotemporally chaotic systems from data: a reservoir computing approach. Phys Rev Lett, 2018, 120: 024102
13 Verstraeten D, Schrauwen B, D'Haene M, et al. An experimental unification of reservoir computing methods. Neural Netw, 2007, 20: 391–403
14 Appeltant L, Soriano M C, van der Sande G, et al. Information processing using a single dynamical node as complex system. Nat Commun, 2011, 2: 468–473
15 Larger L, Soriano M C, Brunner D, et al. Photonic information processing beyond Turing: an optoelectronic implementation of reservoir computing. Opt Express, 2012, 20: 3241–3249
16 Paquot Y, Duport F, Smerieri A, et al. Optoelectronic reservoir computing. Sci Rep, 2012, 2: 287–292
17 Duport F, Schneider B, Smerieri A, et al. All-optical reservoir computing. Opt Express, 2012, 20: 22783
18 Brunner D, Soriano M C, Mirasso C R, et al. Parallel photonic information processing at gigabyte per second data rates using transient states. Nat Commun, 2013, 4: 1364–1370
19 Nguimdo R M, Lacot E, Jacquin O, et al. Prediction performance of reservoir computing systems based on a diode-pumped erbium-doped microchip laser subject to optical feedback. Opt Lett, 2017, 42: 375–378
20 Bueno J, Brunner D, Soriano M C, et al. Conditions for reservoir computing performance using semiconductor lasers with delayed optical feedback. Opt Express, 2017, 25: 2401–2412
21 Kuriki Y, Nakayama J, Takano K, et al. Impact of input mask signals on delay-based photonic reservoir computing with semiconductor lasers. Opt Express, 2018, 26: 5777–5788
22 Nguimdo R M, Erneux T. Enhanced performances of a photonic reservoir computer based on a single delayed quantum cascade laser. Opt Lett, 2019, 44: 49–52
23 Sugano C, Kanno K, Uchida A. Reservoir computing using multiple lasers with feedback on a photonic integrated circuit. IEEE J Sel Top Quantum Electron, 2020, 26: 1–9
24 Koyama F. Recent advances of VCSEL photonics. J Lightw Technol, 2006, 24: 4502–4513
25 Xiang S Y, Ren Z, Zhang Y, et al. All-optical neuromorphic XOR operation with inhibitory dynamics of a single photonic spiking neuron based on VCSEL-SA. Opt Lett, 2020, 45: 1104–1107
26 Vatin J, Rontani D, Sciamanna M. Enhanced performance of a reservoir computer using polarization dynamics in VCSELs. Opt Lett, 2018, 43: 4497–4500
27 Vatin J, Rontani D, Sciamanna M. Experimental reservoir computing using VCSEL polarization dynamics. Opt Express, 2019, 27: 18579–18584
28 Guo X X, Xiang S Y, Zhang Y H, et al. Four-channels reservoir computing based on polarization dynamics in mutually coupled VCSELs system. Opt Express, 2019, 27: 23293–23306

29 Guo X X, Xiang S Y, Zhang Y H, et al. Polarization multiplexing reservoir computing based on a VCSEL with polarized optical feedback. IEEE J Sel Top Quantum Electron, 2020, 26: 1–9

30 Jaeger H. Short term memory in echo state networks. GMD Rep, 2002, 152: 60

31 Inubushi M, Yoshimura K. Reservoir computing beyond memory-nonlinearity trade-off. Sci Rep, 2017, 7: 10199

32 Lazar A, Pipa G, Triesch J. Fading memory and time series prediction in recurrent networks with different forms of plasticity. Neural Netw, 2007, 20: 312–322

33 Hou Y S, Xia G Q, Yang W Y, et al. Prediction performance of reservoir computing system based on a semiconductor laser subject to double optical feedback and optical injection. Opt Express, 2018, 26: 10211–10219

34 Xiang S Y, Zhang Y, Guo X, et al. Photonic generation of neuron-like dynamics using VCSELs subject to double polarized optical injection. J Lightw Technol, 2018, 36: 4227–4234

35 Xiang S Y, Zhang Y, Gong J, et al. STDP-based unsupervised spike pattern learning in a photonic spiking neural network with VCSELs and VCSOAs. IEEE J Sel Top Quantum Electron, 2019, 25: 1–9

36 Tezuka M, Kanno K, Bunsen M. Reservoir computing with a slowly modulated mask signal for preprocessing using a mutually coupled optoelectronic system. Jpn J Appl Phys, 2016, 55: 08RE06

37 Hicke K, Escalona-Moran M A, Brunner D, et al. Information processing using transient dynamics of semiconductor lasers subject to delayed feedback. IEEE J Sel Top Quantum Electron, 2013, 19: 1501610

38 Martin-Regalado J, Prati F, San Miguel M, et al. Polarization properties of vertical-cavity surface-emitting lasers. IEEE J Quantum Electron, 1997, 33: 765–783

39 Jiang N, Pan W, Luo B, et al. Bidirectional dual-channel communication based on polarization-division-multiplexed chaos synchronization in mutually coupled VCSELs. IEEE Photon Technol Lett, 2012, 24: 1094–1096

40 Li N, Susanto H, Cemlyn B R, et al. Stability and bifurcation analysis of spin-polarized vertical-cavity surface-emitting lasers. Phys Rev A, 2017, 96: 013840

41 Deng T, Robertson J, Hurtado A. Controlled propagation of spiking dynamics in vertical-cavity surface-emitting lasers: towards neuromorphic photonic networks. IEEE J Sel Top Quantum Electron, 2017, 23: 1–8

42 Deng T, Robertson J, Wu Z M, et al. Stable propagation of inhibited spiking dynamics in vertical-cavity surface-emitting lasers for neuromorphic photonic networks. IEEE Access, 2018, 6: 67951–67958

43 Jiang N, Zhao A, Xue C, et al. Physical secure optical communication based on private chaotic spectral phase encryption/decryption. Opt Lett, 2019, 44: 1536–1539

44 Nguimdo R M, Verschaffelt G, Danckaert J, et al. Reducing the phase sensitivity of laser-based optical reservoir computing systems. Opt Express, 2016, 24: 1238–1252

45 Guo X X, Xiang S Y, Zhang Y H, et al. Information-theory-based complexity quantifier for chaotic semiconductor laser with double time delays. IEEE J Quantum Electron, 2018, 54: 1–8

46 Wu J G, Xia G Q, Wu Z M. Suppression of time delay signatures of chaotic output in a semiconductor laser with double optical feedback. Opt Express, 2009, 17: 20124

47 Liao Y H, Lin F Y. Dynamical characteristics and their applications of semiconductor lasers subject to both optical injection and optical feedback. Opt Express, 2013, 21: 23568–23578

48 Li N, Susanto H, Cemlyn B, et al. Injection locking of two laterally-coupled semiconductor laser arrays. In: Proceedings of the SPIE, 2018. 106820Z